JACS
JOURNAL OF THE AMERICAN CHEMICAL SOCIETY
pubs.acs.org/JACS
Article

Mechanism of Tyrosine-Driven Deprotonation in Photosystem II Revealed by Multiscale Simulations

Jinchan Liu, Ke R. Yang, Julianne S. Lampert, William H. Armstrong, Gary W. Brudvig, and Victor S. Batista*

Cite This: https://doi.org/10.1021/jacs.5c13000
Read Online

ABSTRACT: Photosystem II (PSII) drives light-induced water oxidation via stepwise redox transitions of its oxygen-evolving complex (OEC), a Mn_4Ca cluster advancing through five intermediate S-states (S_0–S_4). The $S_2 \rightarrow S_3$ transition involves a redox event in which a Mn ion donates an electron to the redox-active tyrosine Y_Z, coupled to deprotonation of an OEC-bound water ligand—yet the underlying coupling mechanism remains unresolved. Time-resolved serial femtosecond crystallography (TR-SFX) has revealed transient electron density shifts near the redox-active tyrosine Y_Z, interpreted as sequential oxidation and reduction, with reduction initiating ∼1 μs after excitation and substantially progressed by 30 μs. However, this interpretation conflicts with kinetics from photothermal beam deflection (PBD), time-resolved X-ray absorption spectroscopy (TR-XAS), and electron paramagnetic resonance (EPR), which place electron transfer at 190–400 μs and proton transfer around 30 μs. Here, we reconcile these discrepancies using quantum mechanics/molecular mechanics (QM/MM) and molecular dynamics (MD) simulations. We show that oxidation of P680 and Y_Z breaks the symmetry of the nearby hydrogen bonds involving water molecule W4, displacing Y_Z and replicating the TR-SFX features of Y_Z and Q165 observed at 1 μs. This local perturbation propagates through a hydrogen-bond network, transmitting the electrostatic signal from Y_Z to the E65-E312 dyad and triggering redox-coupled deprotonation via the Cl1 channel. By 30 μs, the hydrogen-bond symmetry is restored through deprotonation of W2 (or alternatively W1), reproducing the disappearance of TR-SFX density differences around Y_Z and Q165 without requiring Y_Z reduction. Our proposed mechanism also gives molecular insights into the O6* density, assigning it to water reorganization rather than a discrete Ca-bound hydroxide species. Our results reveal a detailed atomistic mechanism linking Y_Z oxidation to long-range proton release and suggest a functional role for the nearby Cl^- ion in proton transfer. More broadly, this study underscores the importance of hydrogen-bond dynamics in mediating redox-driven proton transport and demonstrates how integrative simulations can resolve mechanistic ambiguities.

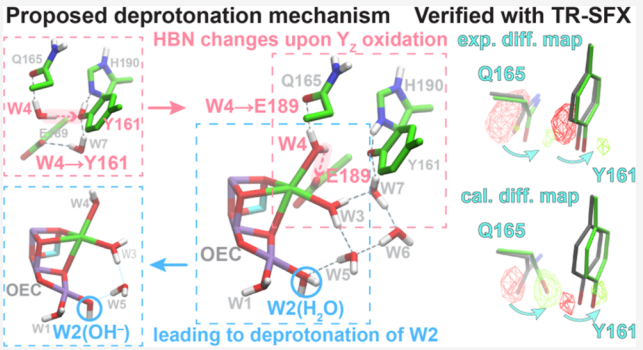

INTRODUCTION

Photosystem II (PSII) is a membrane-bound protein complex that initiates oxygenic photosynthesis by transferring electrons from water to plastoquinone (PQ), a process driven by light absorption of the chlorophyll pigment P680 (Figure 1A).[1−3] On the electron donor side, the oxygen-evolving complex (OEC) (Figure 1B)—a Mn_4CaO_5 cluster—catalyzes the reaction $2H_2O \rightarrow 4H^+ + 4e^- + O_2$ through a series of redox transitions known as the Kok cycle (Figure 1C).[4] During this catalytic cycle, oxidative equivalents are incrementally accumulated in five metastable "storage" states (S_0 to S_4) via alternating electron and proton abstraction steps.[5−7] Unraveling how this light-driven water oxidation occurs under physiological conditions remains a central challenge in biological energy conversion, with broad implications for the development of artificial water-splitting systems and solar fuel technologies.[8−10]

Structural and spectroscopic studies have provided detailed snapshots of the S-state intermediates, particularly S_1 to S_3 (Figure 1D).[11−15] The dark-stable S_1 state, comprising two Mn^{III} and two Mn^{IV} ions bridged by μ-oxo groups and embedded within the protein scaffold, is the entry point to the Kok cycle. High-resolution crystal structures of S_1 not only identify the four water ligands directly coordinating the OEC (W1-W4), but also reveal an extended hydrogen-bond network involving additional waters.[16−19] For example, W5-W7 form a continuous hydrogen-bond chain connecting the OEC to the

Received: July 29, 2025
Revised: February 2, 2026
Accepted: February 5, 2026

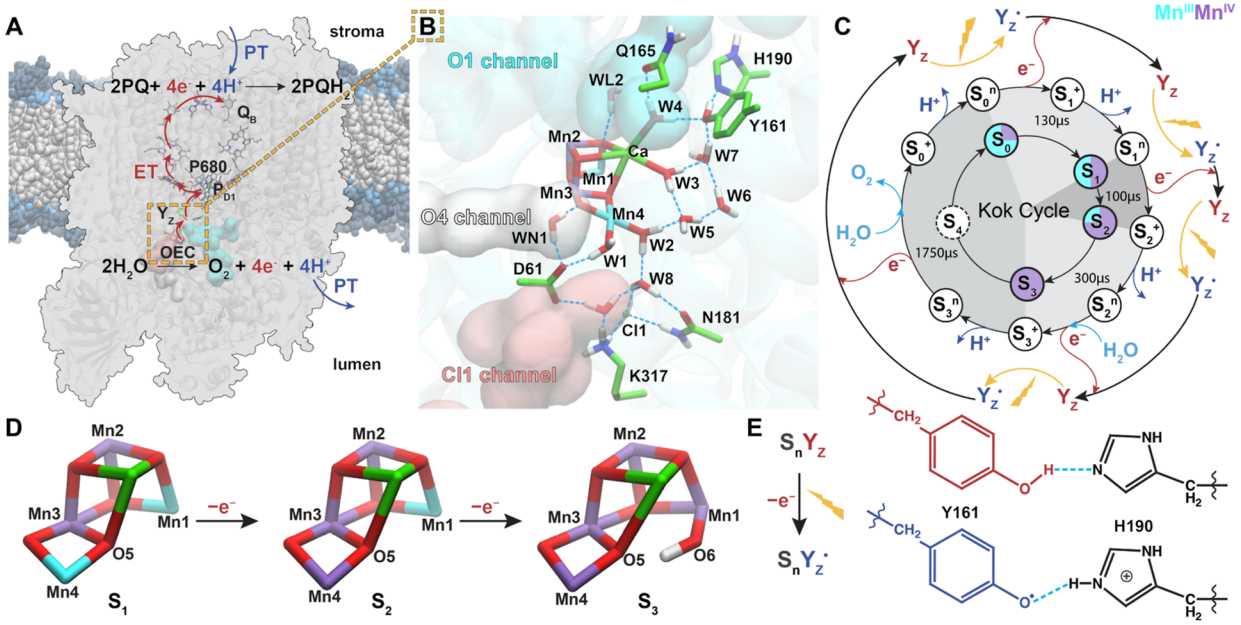

Figure 1. Overview of photosystem II structure, function, and redox cycle. (A) A monomer of photosystem II (PSII, gray) embedded in its native thylakoid membrane, with surrounding lipid molecules shown in van der Waals representation. PSII catalyzes light-driven electron transfer from water to plastoquinone (PQ), with water oxidation occurring at the oxygen-evolving complex (OEC) on the electron donor side. (B) The OEC, an oxo-bridged Mn_4Ca cluster shown in licorice representation, is depicted in the S_1 state. Mn^{III} ions are colored cyan, Mn^{IV} in purple. The OEC is ligated by water and amino acid residues and connected to the protein surface via three water channels, rendered as cyan, white, and pink surfaces. (C) Schematic of the Kok cycle adapted from Dau and Haumann,[86] in which stepwise oxidation by $Y_Z^{\bullet}$ drives transitions between the five redox intermediates (S_0–S_4), culminating in O_2 evolution. The indicated charges (e.g., S_1^n, S_2^+) represent the total charge of the catalytic center, including four Mn ions, five μ-oxo bridges, the Ca ion, six coordinating carboxylates and two substrate waters; the absolute values depend on how the catalytic center is defined and may vary if additional residues are included or if the protonation states of the substrates differ. (D) Computationally derived structures of the open-cubane form of the OEC in the S_1, S_2, and S_3 states, showing progressive oxidation. (E) Proton-coupled electron transfer (PCET) between Y_Z and the adjacent histidine residue H190 forms the $Y_Z^{\bullet}$ radical, which subsequently oxidizes the OEC during each S-state transition. See Table S1 for nomenclature of water molecules involved in OEC coordination and channel connectivity.

redox-active tyrosine Y_Z, while W8 links W2 to the nearby chloride ion Cl1 (Figure 1B). These waters are spatially organized into three main networks—the Cl1, O1, and O4 channels—based on their connectivity and orientation, and are proposed to facilitate substrate delivery and/or proton egress.[20−23] Among these, the Cl1 channel has been most consistently suggested for proton egress, as chloride depletion impairs the $S_2 \rightarrow S_3$ and $S_3 \rightarrow S_0$ transitions, both of which require proton release.[24,25]

With the S_1 state now well-characterized, information for subsequent S-states has become increasingly detailed (Figure 1D). Oxidation of S_1 yields S_2, which contains one additional Mn^{IV} ion relative to S_1, as first identified by electron paramagnetic resonance (EPR)[26−28] and later supported by isomeric spin-coupling models.[29−34] The $S_2 \rightarrow S_3$ transition has been characterized to involve proton release,[35,36] oxidation of a Mn^{III} center,[5−7,37] and the binding of a new water-derived ligand,[38,39] as revealed by kinetic and spectroscopic experiments (Table 1). Computational studies have further examined the mechanisms of deprotonation,[40−45] Mn-oxidation,[41,46−48] water insertion,[41,47,49−51] and the S_3-state geometry.[52−56] While these studies differ in the proposed protonation states of ligand waters and the identity of the water molecule that undergoes deprotonation,[34,42,48] most studies converge on the formation of an additional ligand bound to Mn that completes the cluster's coordination sphere in the S_3 state. Notably, recent time-resolved serial femtosecond crystallography (TR-SFX) using an X-ray free-electron laser (XFEL) has been applied to the $S_2 \rightarrow S_3$ transition.[57−59] These studies directly visualized electron-density features corresponding to this inserted ligand during the $S_2 \rightarrow S_3$ transition,[57,59] providing experimental support for the proposed water-insertion mechanism. Meanwhile, direct crystallographic evidence for the insertion process has been debated.[60,61] After formation of the S_3 state, a lag phase is observed and attributed to a deprotonation step.[5] This is followed by accumulation of a fourth oxidative equivalent, O–O bond formation, and eventual O_2 release.[62−71] Upon O_2 evolution, the OEC resets to the S_0 state, completing one full Kok cycle.[71]

Table 1. Kinetics of the $S_2 \rightarrow S_3$ Transition, Showing Half-Lives and H/D Kinetic Isotope Effects (KIEs) for Proton Transfer (PT, 26–35 μs) and Electron Transfer (ET, 190–400 μs), Depending on Method[5−7,37,82−85]

method[a]	event	τ(μs)	KIE
PBD[6,7]	PT	30, 35	5.6, 4.3
PBD[6,7]	ET	300, 280	1.7, 1.9
XAS[82]	PT	26	4.5
XAS[5,82]	ET	190, 317	1.8
FTIR[37]	Wat Ins	104	1.2
FTIR[37,83]	ET	352, 372	1.9, 2.1
UV(295 nm)[84]	ET	290	-
EPR[85]	ET	400	-

[a]PDB: photothermal beam deflection spectroscopy; XAS: X-ray absorption spectroscopy; FTIR: Fourier-transform infrared spectroscopy; UV(295nm): ultraviolet absorption at 295nm; EPR: electron paramagnetic resonance spectroscopy.

https://doi.org/10.1021/jacs.5c13000
J. Am. Chem. Soc. XXXX, XXX, XXX−XXX

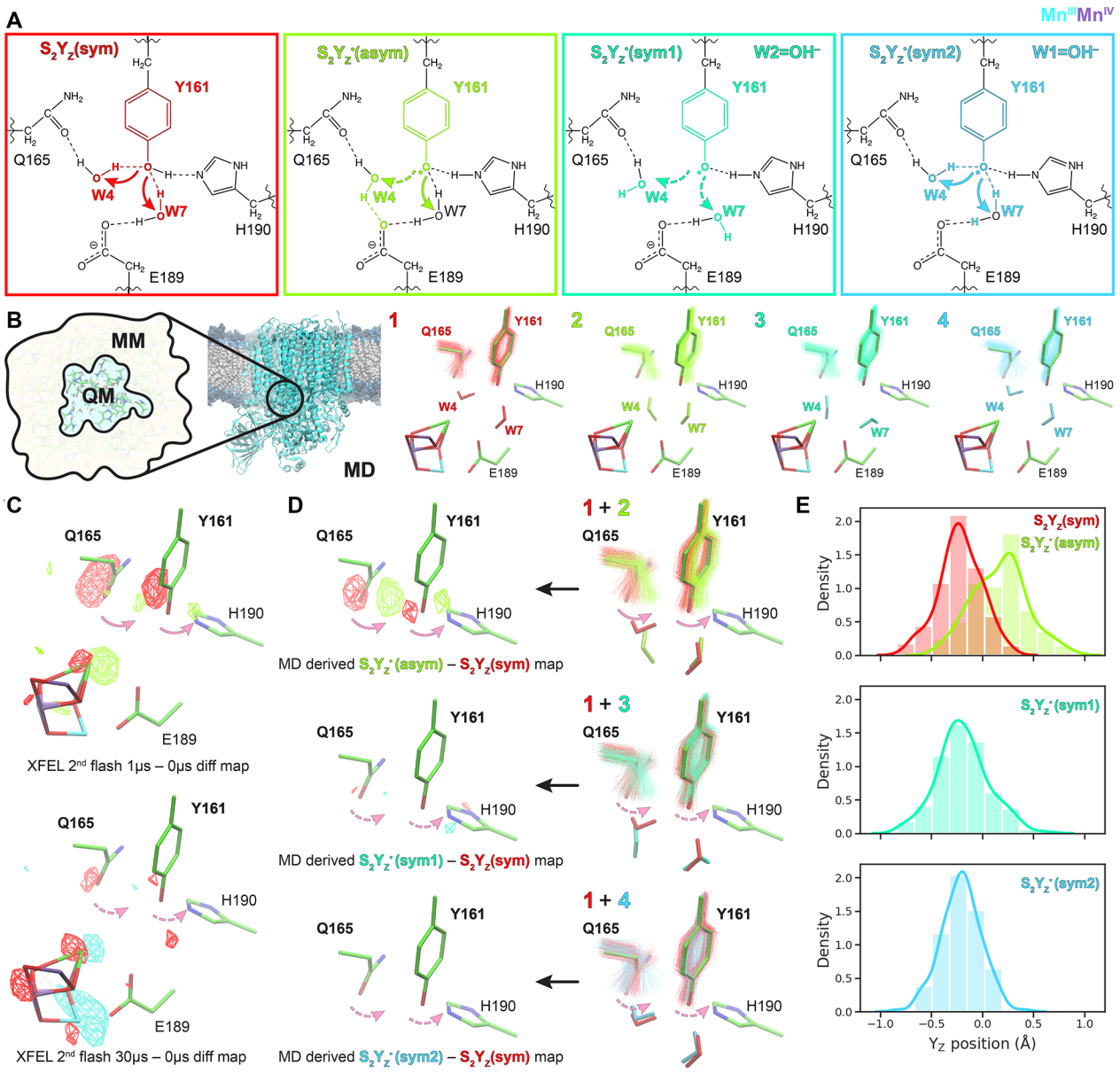

Figure 2. Reconciling TR-SFX and kinetic data with QM/MM assisted MD. (A) Key hydrogen-bonding configurations around Y_Z from QM/MM optimizations. Red box: symmetric configuration with W4 and W7 both donating to Y_Z (State 3A; S_2Y_Z(sym)). Yellow–green box: the electric field from P_{D1}^+ coupled with the reduced charge on the phenolic oxygen of Y_Z (Y161OH) drive W4 rotation toward E189, breaking the symmetry (State 3C*; $S_2Y_Z^{\bullet}$(asym)). Aqua-green and sky-blue boxes: hydrogen-bond symmetry can be restored after deprotonation. Deprotonation of W2 produces a symmetric network with both W4 and W7 reoriented away from $Y_Z^{\bullet}$ (State 3F; $S_2Y_Z^{\bullet}$(sym1)), whereas deprotonation of W1 corresponds to an alternative symmetric configuration with both W4 and W7 donating to $Y_Z^{\bullet}$ ($S_2Y_Z^{\bullet}$(sym2)). (B) QM/MM-MD simulation workflow. Left: QM/MM-optimized states were embedded in a membrane environment for restrained MD simulations that preserve the target hydrogen-bond topology. Right: trajectories with hydrogen-bond restraints to maintain target H-bond states. (C) Experimental TR-SFX difference density maps at 1 and 30 μs after the second flash (0 μs reference, shown in licorice), highlighting the lateral displacements of Y_Z and Q165.[59] Red contours indicate negative difference densities while yellow-green and cyan contours indicate positive difference densities for 1 μs − 0 μs and 30 μs − 0 μs, respectively. (D) MD-derived difference density maps replicate experimental TR-SFX features. Top: the $S_2Y_Z^{\bullet}$(asym) − S_2Y_Z(sym) map captures the lateral displacement of Y_Z and Q165 at 1 μs. Middle and bottom: $S_2Y_Z^{\bullet}$(sym1) − S_2Y_Z(sym) and $S_2Y_Z^{\bullet}$(sym2) − S_2Y_Z(sym) maps reproduce the return to baseline geometry at 30 μs, consistent with hydrogen-bond resymmetrization without Y_Z reduction. (E) Distribution of Y_Z positions sampling from 10 ns of MD, quantified by projecting the $C_\beta \rightarrow$ OH vector of Y161 onto its ring-plane normal in the S_2Y_Z reference geometry.

While the structures of S-states are increasingly well-resolved, the mechanisms underlying the transitions between them remain poorly understood. Each transition is triggered by light-induced charge separation in P680, generating $P680^+$ and resulting in the chlorophyll P_{D1}^+ oxidizing the nearby tyrosine Y161 (Y_Z) (Figure S1).[72−76] This occurs via a proton-coupled electron transfer (PCET) reaction (Figure 1E), in which the tyrosine donates a proton to the adjacent H190 residue and becomes a neutral radical $Y_Z^{\bullet}$, coupled to hydrogen-bond rearrangements (Figure 2A).[77,78] The kinetics of this PCET reaction have been resolved into three phases: a fast nanosecond oxidation of 20−50 ns, a slower nanosecond dielectric relaxation of 300−600 ns, and a 35 μs component associated with further relaxation.[74−76] The resulting $Y_Z^{\bullet}$

https://doi.org/10.1021/jacs.5c13000
J. Am. Chem. Soc. XXXX, XXX, XXX−XXX

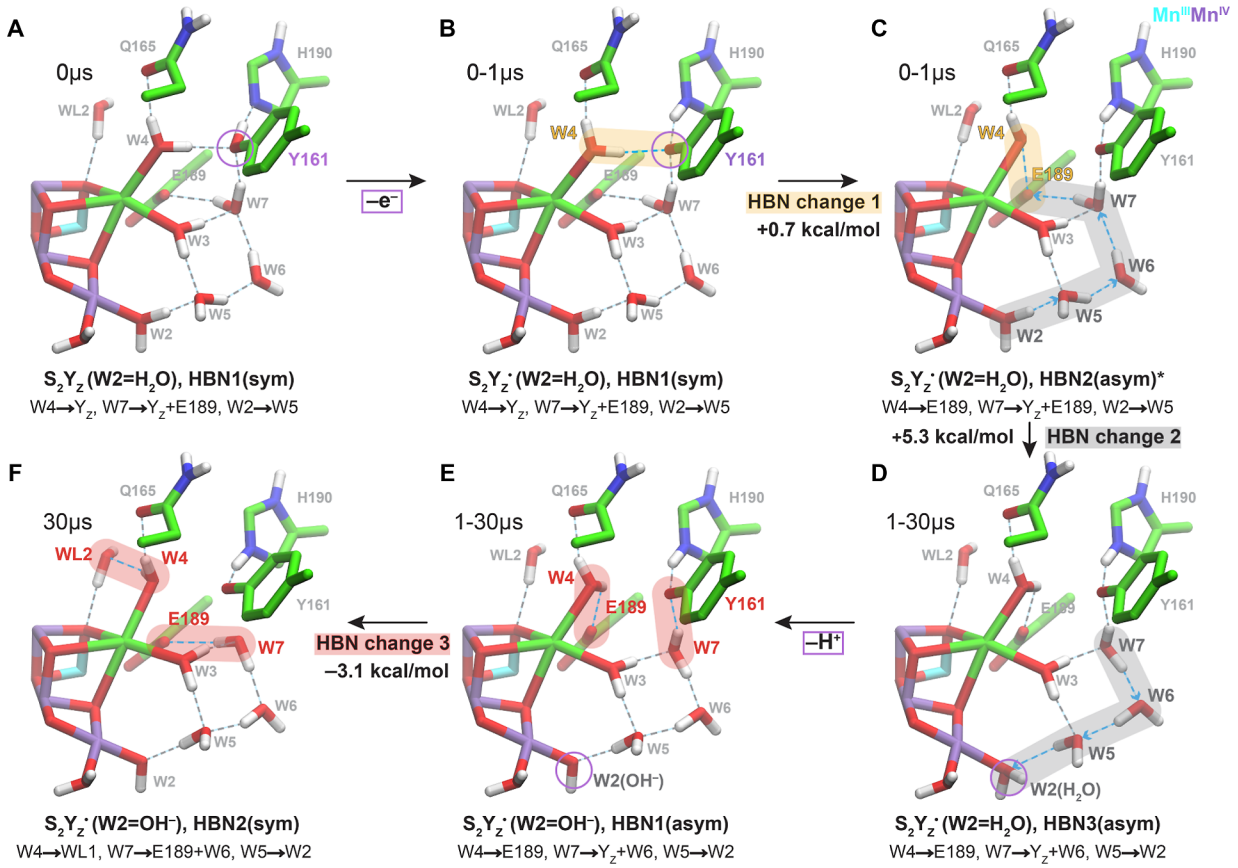

Figure 3. Hydrogen-bond rearrangements triggered by Y_Z oxidation drive redox-coupled deprotonation during the $S_2 \rightarrow S_3$ transition. Three sequential hydrogen-bond network (HBN) changes are highlighted in yellow, gray, and red. (A) S_2Y_Z in its reduced form features symmetric hydrogen bonding from W4 and W7 to Y_Z (HBN1; State 3A). (B) Oxidation of Y_Z to a tyrosyl radical reduces the negative charge on its phenolic oxygen and initiates HBN change 1. (C) W4 reorients away from Y_Z to form a hydrogen bond with E189 (State 3C*), disrupting the W7-E189 interaction and triggering HBN change 2. (D) This initiates a relay of rearrangements through W6 and W5, culminating in W5 donating a hydrogen bond to W2 (State 3D), thereby lowering the pK_a of W2. (E) W2 is deprotonated via the E65-E312 pathway while Y_Z remains oxidized (State 3E). (F) A final rearrangement (HBN change 3) reorients W4 and W7 away from Y_Z, restoring hydrogen-bond symmetry in the deprotonated state (State 3F). All structures shown are QM/MM-optimized; states marked with * exhibit a small imaginary frequency, consistent with metastable intermediates.

radical then oxidizes the OEC by abstracting an electron from one of the Mn ions—though the exact Mn site depends on the specific S-state transition.[79−81] Upon reduction, the $Y_Z^{\bullet}$ radical reclaims the proton from H190, returning to its neutral form in preparation for the next redox transition. This stepwise accumulation of oxidative equivalents drives forward progression through the Kok cycle and enables sustained catalytic turnover.

Building on this framework, a recent TR-SFX study using an XFEL reported significant electron density changes around Y_Z during the $S_1 \rightarrow S_2$ and $S_2 \rightarrow S_3$ transitions (Figure 2C).[59] These transient features appeared shortly after photoexcitation and disappeared over defined time intervals by the end of each transition. Li et al. attributed the appearance of these features to Y_Z oxidation and their disappearance to its subsequent reduction by the OEC.[59] Specifically, during the $S_2 \rightarrow S_3$ transition, they reported: "At Δt_2 = 30 μs, difference densities on Y_Z and D1-Q165 decrease, indicating the re-reduction of $Y_Z^{\bullet}$ by the OEC. The difference density on Y_Z becomes even weaker at Δt_2 = 200 μs, but is still present." This interpretation implies that electron transfer (ET) from the OEC to $Y_Z^{\bullet}$ initiates around 1 μs, proceeds substantially by 30 μs, and continues through at least 200 μs. It further supports a sequential mechanism in which Y_Z oxidation, reduction, and water ligand insertion (O6) occur in series.

However, assigning the disappearance of these difference densities to $Y_Z^{\bullet}$ reduction implies a faster ET step than previously observed (Table 1). This stands in contrast to a broad range of kinetic studies, which consistently place the ET step in the $S_2 \rightarrow S_3$ transition at later times: 280−300 μs from photothermal beam deflection (PBD),[6,7] 190−317 μs from time-resolved X-ray absorption spectroscopy (TR-XAS),[5,82] 352−372 μs from time-resolved Fourier transform infrared spectroscopy (FTIR),[37,83] 290 μs from UV absorbance at 295 nm,[84] and 400 μs from EPR.[85] If the ET half-time is in the 300−400 μs range, only a small fraction of $Y_Z^{\bullet}$ should be reduced by 30 μs—far less than implied by the TR-SFX electron density loss—raising a mechanistic inconsistency.

Moreover, our prior QM/MM work showed that O6 insertion into the OEC lowers its reduction potential, thereby favoring Mn-oxidation and $Y_Z^{\bullet}$ reduction—implying that the tyrosyl radical should persist until after O6 binding to the Mn occurs.[47] The TR-SFX-based interpretation, which posits earlier $Y_Z^{\bullet}$ reduction, complicates this picture. Although several computational studies have explored water delivery and deprotonation in the $S_2 \rightarrow S_3$ transition, few have

https://doi.org/10.1021/jacs.5c13000
J. Am. Chem. Soc. XXXX, XXX, XXX−XXX

reconciled their predictions with experimental kinetics or addressed conflicting interpretations across spectroscopic and structural methods.

Here, we address this gap by combining quantum mechanics/molecular mechanics (QM/MM) and molecular dynamics (MD) simulations to analyze structural changes that correlate with the TR-SFX difference densities observed at 1 and 30 μs following the second flash. Our simulations reveal a cascade of hydrogen-bond rearrangements initiated by Y_Z oxidation, culminating in a redox-coupled deprotonation step that occurs before electron transfer. This model explains the disappearance of TR-SFX difference density features by 30 μs and aligns with experimental proton transfer (PT) kinetics from PBD and TR-XAS, which place proton transfer in the 26−35 μs range.[6,7,82] These findings offer a unified mechanistic framework that reconciles time-resolved structural data with multitechnique kinetic measurements.

RESULTS AND DISCUSSION

Tyrosine Oxidation Induces Hydrogen-Bond Asymmetry

To investigate the molecular origin of the TR-SFX difference densities observed near Y_Z (Figure 2)—specifically, the rightward shift of the tyrosine side chain at 1 μs and its return by 30 μs (Figure 2C)—we performed QM/MM optimizations initiated from the S_2Y_Z reference state. This state (State 3A; Figure 3A) exhibits a symmetric hydrogen-bonding network (HBN1), with both W4 and W7 donating hydrogen bonds to the phenolic oxygen of Y_Z (Y161OH), effectively pulling it in opposite directions (S_2Y_Z(sym); Figure 2A, red box).

Structural analysis revealed that W4, Y161OH, and the central magnesium of the accessory chlorophyll P_{D1}—the site of positive charge following charge separation—are nearly colinear and separated by a hydrophobic bridge composed of V157, I290, M293, F186, F182, I192, and M183 (Figure S1). This arrangement forms a low-dielectric "conductor" (with $\varepsilon \approx 2-4$),[87,88] which enables efficient transmission of the electric field from P_{D1}^+ to the W4 → Y_Z hydrogen bond prior to Y_Z oxidation. This electric field is oriented nearly antiparallel (158°) to the W4 → Y_Z hydrogen bond vector, making this interaction electrostatically unfavorable immediately after charge separation.

We propose that the destabilized interaction promotes reorientation of W4 away from Y_Z and association with a new hydrogen bond acceptor, E189 (HBN2), which in turn facilitates oxidation of Y_Z (Figure S3). To quantify this coupling, we analyzed Y_Z oxidation in configurations differing by the hydrogen bond partner of W4, starting from the optimized symmetric S_2Y_Z state, State 3A. We then optimized the oxidized state $S_2Y_Z^\bullet$ maintaining symmetric HBN1 with both W4 and W7 hydrogen bonding to Y_Z (State 3B; Figure 3B). In parallel, we obtained configurations in which W4 reorients to E189, breaking the symmetry of hydrogen bonding around Y_Z, in both the reduced (S_2Y_Z, W4 → E189) and oxidized state ($S_2Y_Z^\bullet$, W4 → E189; State 3C*; Figure 3C). The results show that when W4 donates to E189 rather than Y_Z, oxidation is favored by 4.3 kcal/mol relative to the symmetric configuration ($\Delta E(Y_Z$ ox, W4 → $Y_Z) - \Delta E(Y_Z$ ox, W4 → E189) = 4.3 kcal/mol), indicating that W4 reorientation promotes electron transfer from Y_Z to P_{D1}^+.

Conversely, Y_Z oxidation reduces the negative charge on its phenolic oxygen (−0.89 → −0.74; Figure S2), thereby weakening its hydrogen-bond acceptor strength, consistent with studies by Nakamura et al.[77,78] With its hydrogen bond to Y_Z destabilized, W4 reorients toward E189. Energetically, W4 → Y_Z is favored by 5.0 kcal/mol at S_2Y_Z, but the two configurations become nearly isoenergetic (+0.7 kcal mol/mol) upon Y_Z oxidation (State 3B vs 3C*). Thus, the shift of hydrogen bond equilibrium and the oxidation of Y_Z act cooperatively: the transient electric field generated by P_{D1}^+ perturbs the hydrogen-bond network toward an asymmetric configuration, shifting the position of Y_Z and accelerating its oxidation, and oxidation in turn stabilizes the asymmetric configuration. This reciprocal coupling between Y_Z oxidation and hydrogen-bond symmetry breaking results in a configuration of $S_2Y_Z^\bullet$(asym) (Figure 2A, yellow-green box), providing a mechanistic basis for the transient Y_Z displacement observed at 1 μs in the TR-SFX data (Figure 2D).

Because the TR-SFX difference densities near Y_Z vanish by 30 μs, we hypothesized that hydrogen-bond symmetry is restored at this time point (Figure 2A, aqua-green and sky-blue boxes). Given that proton abstraction kinetics assign a half-life of 30 μs to deprotonation,[6,7,82] we propose that resymmetrization arises from deprotonation rather than Y_Z reduction. Deprotonation can in principle occur at several candidate sites, including W1, W2, W3, D61, and E312, which are connected through the OEC and the proposed K317−Cl1 proton-release network. These potential sites are not mutually exclusive: for instance, W3 insertion coupled with a deprotonation requires a predeprotonated W2 to accept a proton,[41] whereas E312 deprotonation can be refilled via a D61-mediated pathway.[44] The Ca-bound O6* reported by Li et al. has also been proposed to be deprotonated. However, our electronic-structure calculations indicate that a deprotonated H_2O at this position is not stable (Figure S5). Because WL2 (corresponding to W28 in the Berkeley model) has been proposed to be the origin of O6*,[59] we modeled WL2 as an OH^- located at the position where O6* is observed, 2.2 Å from Ca. Single-point calculations yielded a spin density around 0.8 on the OH^- (Figure S5A), indicating that it would be oxidized by $Y_Z^\bullet$ rather than remaining a closed-shell anion. Geometry optimization further confirmed the instability of this configuration (Figure S5B,C), excluding the possibility of a stable OH^- species at this position.

In this study, we therefore focused on deprotonation of W1 and W2, which are directly coupled to Y_Z via a hydrogen bond relay W5-W6-W7. We modeled $S_2Y_Z^\bullet$ with both W1 = OH^- and W2 = OH^- (Figure S4) and identified a symmetric hydrogen-bonding pattern for each state. W2 = OH^- (State 3F; Figure 3F) is more favorable in a configuration where both W4 and W7 reorient away from Y_Z ($S_2Y_Z^\bullet$(sym1); Figure 2A, aqua-green box), as the W5-W6-W7 relay points to W2 when it is a hydroxide (Figure S6). In contrast, W1 = OH^- (State S4; Figure S4) enables a configuration in which both W4 and W7 hydrogen bond to Y_Z ($S_2Y_Z^\bullet$(sym2); Figure 2A, sky-blue box), because the W2-W5-W6-W7 relay remains oriented toward Y_Z when W2 is neutral. Although W2 = OH^- is more favorable then W1 = OH^- by 2.7 kcal/mol (Figure S4), both configurations were included to assess whether their predicted structural rearrangements reproduce the experimental TR-SFX difference densities.

To evaluate whether the proposed rearrangements account for the experimental TR-SFX difference densities, we performed MD simulations initiated from QM/MM-derived structures corresponding to State 3A (S_2Y_Z(sym)), State 3C* ($S_2Y_Z^\bullet$(asym)), State 3F ($S_2Y_Z^\bullet$(sym1)), and State S4

https://doi.org/10.1021/jacs.5c13000
J. Am. Chem. Soc. XXXX, XXX, XXX−XXX

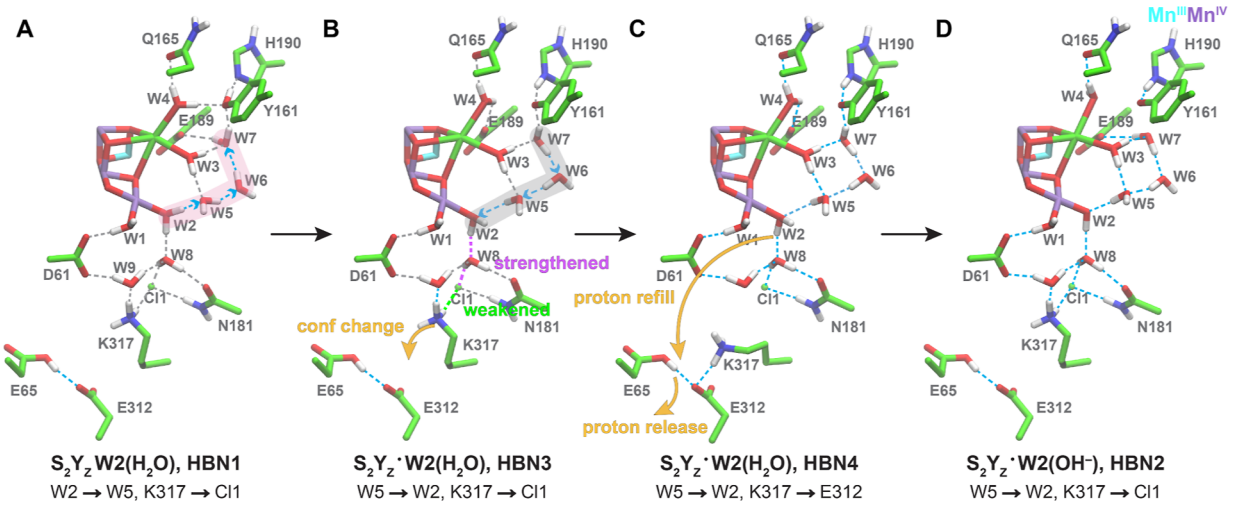

Figure 4. Proposed role of Cl1 in mediating redox-coupled deprotonation. (A) Initial hydrogen-bond network in the reduced state (S_2Y_Z with W2 = H_2O; State 3A), featuring W2 → W5 hydrogen bond and a salt bridge between K317 and Cl1. (B) Upon Y_Z oxidation ($S_2Y_Z^\bullet$, W2 = H_2O; State 3D), a W5 → W2 hydrogen bond is established, lowering the pK_a of W2. This strengthens the W2 → W8 → Cl1 hydrogen-bond relay and weakens the K317−Cl1 salt bridge, facilitating reorientation of K317. (C) K317 reorients to form a salt bridge with E312, promoting proton release from the E65-E312 dyad and potential proton refill from W2. (D) Final state following deprotonation (W2 = OH^-; State 3F). This model suggests a mechanism by which Cl1 senses and modulates local electrostatics, coupling Y_Z oxidation to long-range proton release. The structures shown here are assembled from QM/MM and MD snapshots to illustrate a mechanistic hypothesis. As E65 and E312 lie at the edge of our current QM/MM system, electrostatic accuracy in this area is limited, and further calculations with an expanded QM region and MM region will be needed to test this proposal.

($S_2Y_Z^\bullet$(sym2)) with hydrogen-bond restraints derived from the QM/MM optimizations (Figure 2B).

Trajectory analysis revealed that in S_2Y_Z, Y161 remains centered near its initial position. In contrast, in $S_2Y_Z^\bullet$(asym), Y161 shifts rightward, consistent with the 1 μs TR-SFX map (Figure 2C). Q165 exhibits a coordinated rightward displacement in this state, maintaining a hydrogen bond with W4, which has reoriented toward E189. This rearrangement of the hydrogen-bonding network explains the concerted movement of both Y161 and Q165 observed experimentally (Figure 2C). In $S_2Y_Z^\bullet$(sym1/2), Y161 returns to its original position, while Q165 remains slightly displaced and displays increased positional variability. Computed difference density maps, $S_2Y_Z^\bullet$(asym) minus S_2Y_Z(sym), and $S_2Y_Z^\bullet$(sym1/2) minus S_2Y_Z(sym), closely resemble the experimental TR-SFX maps at 1 μs and 30 μs, respectively (Figure 2D). The positional distributions of Y_Z are nearly identical among all symmetric states, whereas only the asymmetric hydrogen-bond configuration produces a measurable displacement of Y_Z (Figure 2E). Additional TR-SFX features not addressed here are discussed in Supporting Information Text 1.

Our electron density calculations in Figure 2 do not explicitly include solvent waters, as water densities arise from collective dynamics, including exchange, diffusion, and flexibility, on time scales beyond our sampling. Nevertheless, our calculations provide clues to the molecular origin of the O6* density observed at 1 and 30 μs. First, the position of O6* lies between W4 and WL2 (2.14 and 2.42 Å away, respectively; Figure S7A), well below typical O ··· O distances in liquid water,[89] implying that O6* is unlikely to represent a distinct water molecule. Instead, it may arise from a more continuous W4-WL2 distribution that forms as Y_Z oxidation weakens its hydrogen-bond acceptor capacity and thus ability to anchor waters (Figure S2), allowing them to become more dynamic, diffuse, and delocalized. Second, W4 maintaining hydrogen bonds with Q165 and E189 upon Y_Z oxidation shifts its position toward the observed O6* density in our MD calculations (Figure S7). This sampling yields an average W4−Ca distance of 2.24 ± 0.05 Å, compared to 2.31 ± 0.12 Å when Y_Z remains reduced (Figure S8). Although a modest change, it is consistent with the trend of observed in TR-SFX: in the TR-SFX structures, the Ca−O6* distance (2.2 Å) is shorter than the 2.4−2.6 Å typical for W3 or W4 coordination, which originally motivated interpreting O6* as a hydroxide. Our calculations reproduce this shorter Ca−O6* distance without invoking an unstable hydroxide species (Figure S5). Third, if O6* were a stable OH^- at 30 μs, W4 would be expected to donate a hydrogen bond to it, since hydroxide is a stronger hydrogen-bond acceptor than Y_Z or E189. Meanwhile, with W2 remaining protonated, the W2-W5-W6-W7 relay would direct W7 toward Y_Z, maintaining an asymmetric hydrogen-bond network and preventing the disappearance of Y_Z difference density at 30 μs. In summary, these observations indicate that O6* is unlikely to correspond to an independent deprotonated OH^- species, but rather reflects a transient, delocalized water configuration that accompanies Y_Z oxidation and relaxation of the surrounding network.

Together, these results support a model in which oxidation of P_{D1} and Y_Z induces symmetry breaking in the local hydrogen-bonding network, while deprotonation of W2 or W1 restores symmetry—linking structural dynamics observed by TR-SFX with known kinetic intermediates (Figure 2C). More broadly, this combined QM/MM-MD approach reveals proton-coupled motions that remain invisible to current TR-SFX resolution limits, providing a mechanistic framework for interpreting transient, sub-Ångström-scale structural changes in time-resolved experiments.

Redox-Coupled Hydrogen-Bond Rearrangements Drive Proton Release in the $S_2 \rightarrow S_3$ Transition

Having established that the TR-SFX difference densities at 1 and 30 μs reflect dynamic changes in hydrogen bonding

https://doi.org/10.1021/jacs.5c13000
J. Am. Chem. Soc. XXXX, XXX, XXX−XXX

around Y_Z, we next examined how these rearrangements relate to deprotonation kinetics (Table 1). We propose a multistep, redox-coupled mechanism in which oxidation-induced reorganization of the HBN progressively lowers the proton affinity of the W2 ligand, ultimately enabling its deprotonation via the Cl1 channel (Figures 3 and 4).

The process initiates from the S_2Y_Z state with a symmetric HBN1 configuration (State 3A; Figure 3A), where both W4 and W7 donate hydrogen bonds to the phenolic oxygen of Y_Z. Upon oxidation of P_{D1} and Y_Z (State 3B; Figure 3B), this symmetry is disrupted by the electrostatic repulsion from P_{D1}^+ prior to Y_Z oxidation and diminished negative charge on Y161OH upon Y_Z oxidation. Together, these factors promote reorientation of W4 away from Y_Z.

In the resulting asymmetric configuration (State 3C*; Figure 3C), W4 forms a new hydrogen bond with E189. Because E189 is directly coordinated to Ca^{2+}, its carboxylate charge is partially delocalized, reducing its basicity and weakening its capacity to act as a hydrogen bond acceptor. This yields a metastable configuration in which E189 accepts hydrogen bonds from both W4 and W7. This state was optimized by constraining the hydrogen bond between W4 and E189, and the structure exhibits a small imaginary vibrational frequency (-83.3 cm^{-1}), with W4 oscillating about E189, indicating strain within the local HBN.

To relieve this strain, the W7-E189 hydrogen bond reorients, initiating a relay of hydrogen-bond rearrangements that propagates through W7-W6-W5 and reaches the $Mn4^{IV}$-bound W2 ligand (State 3D; Figure 3D). Despite preserving the overall number of hydrogen bonds, this reorganization raises the system energy by 5.3 kcal/mol, as it forces W2, normally a terminal ligand, to accept a hydrogen bond from W5. The resulting W5 → W2 interaction destabilizes W2, consistent with TR-SRX observations showing transient weakening of W2 electron density at 1 μs.[59] Receiving this hydrogen bond decreases the proton affinity of W2, as indicated by a shortened W2 → W8 hydrogen bond (2.67 → 2.58 Å; Table 2) triggered by Y_Z oxidation (Figure S9).

Table 2. Important Distances in Å of States of 3A-F from Our QM/MM Optimizations

	3A	3B	3C	3D	3E	3F
Y161OH-H190NE2	2.48	2.68	2.67	2.68	2.66	2.69
W4-Y161OH	2.72	2.80	3.11	3.01	2.99	3.11
W4-Q165OE1	2.81	2.76	2.81	2.80	2.88	2.86
W4-E189OE1	3.15	3.13	2.71	2.72	2.69	2.84
W7-Y161OH	2.67	2.80	2.75	2.74	2.77	2.85
W7-E189OE1	2.90	2.80	2.84	3.24	3.28	2.95
W1-D61	2.61	2.58	2.59	2.59	2.66	2.67
W2-W8	2.67	2.65	2.66	2.58	2.77	2.77
W8-Cl1	3.19	3.18	3.18	3.05	3.20	3.21
K317NZ-Cl1	3.15	3.17	3.17	3.20	3.15	3.15

Concurrently, the W1-D61 distance decreases slightly (2.61 → 2.59 Å; Table 2), reflecting a small electrostatic response and suggesting that W1 may serve as an alternative deprotonation site, consistent with previous studies that proposed Y_Z oxidation can promote proton transfer from W1.[40,42,48] We favor W2 as the intermediate that completes the deprotonation pathway, however, because it is 2.7 kcal/mol more favorable, with a smaller estimated pK_a.[90]

Tightly associated with the strengthened W2 → W8 hydrogen bond, we observe a corresponding shortening of the W8−Cl1 distance (3.19 → 3.05 Å) and a slight weakening of the adjacent K317−Cl1 salt bridge (3.15 → 3.20 Å) (Figure S9). These correlated changes indicate that the electrostatic perturbation initiated by Y_Z oxidation propagates through W2 and W8 to reach the Cl1 site. Chloride, long recognized as essential for efficient S-state transitions in PSII, with Cl^- depletion known to impair both the $S_2 \rightarrow S_3$ and $S_3 \rightarrow S_0$ transitions,[24,25] thus appears to act here as an electrostatic sensor, responding to redox-driven changes at Y_Z.

We propose that this response enables Cl1 to serve as a signal transmitter that couples the oxidation event at Y_Z to proton release. Specifically, weakening of the K317−Cl1 salt bridge may permit K317 to reorient toward E312 and facilitate proton release from the E312-E65 dyad,[45] as suggested by alternative K317 conformations observed in cryo-EM structures,[91,92] thereby relaying the electrostatic signal to the distal proton-release site.[44] Proton removal from the E312-E65 dyad would then require refilling from the hydrogen-bond network proximal to the OEC, most likely through deprotonation of W1 or W2. These two events need not be mutually exclusive: W1 may transiently donate a proton to D61, replenishing the E312-E65 dyad, while W2 subsequently refills W1, consistent with its 2.7 kcal/mol energetic advantage. Overall, W8 functions as a polar bridge connecting W2 to Cl1, while Cl1 operates as both an electrostatic sensor and modulator, transmitting the redox signal from Y_Z oxidation to the E312-E65 proton-release dyad. This mechanism explains how proton release can originate from a site 18 Å away from Y_Z, underscoring the long-range coupling between redox chemistry and proton transport in PSII.

The resulting deprotonated intermediate (W2 = OH^-; State 3E; Figure 3E) still exhibits asymmetric hydrogen bonding around Y_Z, with W7 donating a hydrogen bond and W4 rotating away. This configuration remains consistent with the intermediate electron density features observed at 1 μs. Finally, the system relaxes into a lower-energy symmetric state (State 3F; Figure 3F), in which both W4 and W7 reorient away from Y_Z, restoring hydrogen-bond symmetry (Figure S6). This final rearrangement (HBN change 3) lowers the system's energy by 3.1 kcal/mol and corresponds to the disappearance of Y_Z and Q165 TR-SFX difference density features at 30 μs. At the same time, the density of W7 weakens, as W7 reorients away from Y_Z, losing its amino acid anchor and becoming more dynamic (Figure 2C).

This multistep model aligns with prior kinetic studies of P_{D1}^+ decay, which reveal three distinct phases: (i) a fast nanosecond component corresponding to direct Y_Z oxidation, (ii) a slower nanosecond phase attributed to dielectric relaxation, and (iii) a 35 μs phase associated with further relaxation.[74−76] We propose that the second, slower nanosecond phase reflects hydrogen-bond network (HBN) change 1, in which the reorientation of W4 occurs in response to the antiparallel electric field generated by P_{D1}^+, facilitating the oxidation of Y_Z. This rearrangement stabilizes the $Y_Z^\bullet$ radical and accounts for the lateral displacement of Y_Z observed in the 1 μs TR-SFX data. The third kinetic phase, at 35 μs, may correspond to subsequent HBN rearrangements or to the deprotonation event itself—both of which redistribute local electrostatics and facilitate electron transfer from Y_Z to P_{D1}^+.

Our proposed long-range proton-transfer mechanism reconciles the TR-SFX data with the large kinetic isotope

https://doi.org/10.1021/jacs.5c13000
J. Am. Chem. Soc. XXXX, XXX, XXX−XXX

effects (KIE = 4.3−5.6) observed at 26−35 μs,[6,7] which indicate a rate-limiting proton-transfer step preceding electron transfer. The smaller KIEs of 1.9 and 2.1 reported by Sakamoto et al., Sugie et al. at 352−372 μs do not contradict this interpretation, as they likely correspond to subsequent PCET events.[37,83] For example, the oxidation mechanism proposed by Allgöwer et al. involves transferring a proton on W3 to W2.[41] Alternatively, proton transfer from W1 to D61 may modulate the reduction potential of the Mn center, as proposed by Yang et al.[32] Our previous calculations support this by showing the S_3-open conformation is more favorable when W1 is deprotonated with its proton residing on D61, whereas before oxidation the configuration was with W1 = H_2O.[47]

Although our calculations were performed for the open-cubane conformation, the electrostatic environment governing Y_Z and Q165 dynamics should remain largely unaltered in the closed-cubane form, implying that the same TR-SFX density changes would be observed. In the closed-cubane configuration, a deprotonated W2 could be inserted into the cluster, as we previously suggested.[47] However, it is also possible that W3 is inserted into the open-cubane structure, as suggested by Allgöwer et al., Kim and Debus, with W3 simultaneously transferring its proton to W2.[41,93] These possibilities do not conflict with the O6* density, which was interpreted as the origin of water insertion. In fact, our simulations reproduce a similar electron density to O6* from purely hydrogen-bond reorganization, without requiring formation of a Ca-bound hydroxide (Figure S7).

Overall, our deprotonation mechanism shows strong consistency with the experimental TR-SFX data, accounting for the observed densities of O6*, Y161, Q165, and W7 at 1 and 30 μs. Both W1 and W2 deprotonation can reproduce the Y161 and Q165 difference densities, and these two routes need not conflict; we favor W2 because of its lower computed free energy and the smaller pK_a estimated by Kaur et al.[90] Moreover, deprotonation of W1 would make subsequent water insertion more difficult, as it lies farther from the potential ligand-binding sites.

We greatly appreciate the hard and rigorous work of Li et al. in revealing these transient densities, and our study complements their findings by providing a mechanistic interpretation that reconciles structural and kinetic observations. Our approach demonstrates how QM/MM-assisted MD can be used to interpret subtle TR-SFX features, while also highlighting its limitations. Specifically, the need for restraints in MD and the artifacts it may introduce. Future ab initio MD simulations, although computationally demanding for a system of this size and time scale, could provide a more rigorous description of water dynamics and a detailed picture of proton transfer. More broadly, our results underscore both the promise and the challenge of interpreting time-resolved densities: these maps are precious and powerful, but inherently ambiguous, requiring interpretations that are at once careful and imaginative, integrating complementary experimental and computational evidence.

In summary, our data support a model in which Y_Z oxidation initiates a cascade of spatially coordinated hydrogen-bond reorganizations that culminate in long-range proton release. Whereas earlier models invoked a generic electrostatic influence of $Y_Z^{\bullet}$, our findings provide a mechanistic framework by which redox-induced electrostatics are propagated through a dynamic hydrogen-bonding network with atomistic specificity.

Evidence in the $S_2 \rightarrow S_3$ Transition Supports the Proton-Rich Model

Our reinterpretation of the TR-SFX signal at 30 μs suggests that the observed disappearance of difference density reflects the completion of a deprotonation event early in the $S_2 \rightarrow S_3$ transition. In combination with TR-SFX features at 200 μs—indicating insertion of a new ligand into the oxygen-evolving complex (OEC)—these data support a mechanistic sequence in which deprotonation precedes substrate water insertion.

A key uncertainty in verifying this mechanism computationally lies in the initial protonation state of the OEC, specifically whether W2 is protonated (H_2O) or already deprotonated (OH^-) at the start of the S_2 state. To address this, we evaluated two alternative protonation schemes: (1) a proton-rich model, in which W2 begins as H_2O and is deprotonated during the transition; and (2) a proton-depleted model, in which W2 is already OH^- in the S_2 state, implying that another water ligand must be deprotonated during $S_2 \rightarrow S_3$.

Within the proton-rich model, we explored two mechanistic routes starting from an initial configuration in which both W1 and W2 are H_2O (P1; Figure S10A). In the first route, W2 is first deprotonated to form P2 (W1 = H_2O, W2 = OH^-), and either the resulting OH^- is inserted into the OEC, or other water is inserted transferring its proton to W2, occupying the coordination site at Mn1 ($S_2Y_Z^{\bullet}$ + H_2O, P2). The vacated W2 site is then replenished by an incoming water molecule. In the second route, water insertion precedes deprotonation: a water molecule (WI) is inserted into the OEC while both W1 and W2 remain as H_2O, yielding a $S_2Y_Z^{\bullet}$ + H_2O configuration (W1 = W2 = WI = H_2O). WI is subsequently deprotonated to form the OH^- ligand.

Both pathways converge on the same final intermediate ($S_2Y_Z^{\bullet}$ + H_2O, P2), in which an OH^- ligand is coordinated to Mn1—originating either from deprotonated W2 or from WI. QM/MM calculations show that the W2-deprotonation-first is energetically favored by 3.4 kcal/mol ($\Delta E_2 - \Delta E_1$), consistent with the experimentally observed TR-SFX sequence and supporting a mechanistic order in which deprotonation precedes water insertion.

In the proton-depleted model, W2 is assumed to begin as OH^- in the $S_2Y_Z^{\bullet}$ state, with W1 = H_2O (P2; Figure S10B). This initial configuration is equivalent to the postdeprotonation intermediate of the proton-rich set ($S_2Y_Z^{\bullet}$, P2). From this starting point, we explored two mechanistic alternatives: (i) direct deprotonation of W1 to form P3 (W1 = W2 = OH^-); and (ii) insertion of a new water ligand (WI), yielding $S_2Y_Z^{\bullet}$ + H_2O with W2 = OH^- and WI = H_2O. Both pathways converge on a common final state (P3), in which both W1 and WI are deprotonated. However, in this case, the insertion-first route is energetically favored by 8.16 kcal/mol ($\Delta E_4 - \Delta E_3$), contradicting the TR-SFX timeline and the mechanistic requirement that deprotonation precedes water insertion.

Additional evidence supports the proton-rich model over the proton-depleted one. Prior studies[42,48] also suggested both W1 and W2 should be H_2O at S_2 state. Furthermore, calculations of hyperfine coupling constants for W1 and W2 in the proton-rich configuration yield values consistent with experimental EPR data for the S_2 state—especially when W2 is modeled as H_2O and W1 as H_2O engaged in a shared-proton interaction with D61.[32] In contrast, modeling W2 as OH^- should produce

https://doi.org/10.1021/jacs.5c13000
J. Am. Chem. Soc. XXXX, XXX, XXX−XXX

hyperfine couplings that are too large to reconcile with experiment. Finally, the proton-depleted model implies that one of W1 or W2 is already deprotonated in the S_1 state, resulting in an OH^- ligand bound to Mn_4^{III}. This coordination is chemically disfavored: Mn(III) centers with carboxylate and oxo ligands are insufficiently Lewis acidic to deprotonate water at near-neutral pH, and Mn(III)−OH^- complexes are rarely observed in synthetic systems.[94] Taken together, these energetic, spectroscopic, and chemical restraints strongly support the proton-rich model as the more realistic representation of the OEC's protonation state in S_2.

CONCLUSIONS

In this study, we present a mechanistic model for deprotonation during the $S_2 \rightarrow S_3$ transition in Photosystem II that reconciles structural insights from time-resolved serial femtosecond crystallography (TR-SFX) with complementary kinetic data. Using a combination of quantum mechanics/molecular mechanics (QM/MM) and molecular dynamics (MD) simulations, we reproduce the electron density changes observed around Y_Z in TR-SFX experiments and propose that these reflect a cascade of redox-triggered hydrogen-bond rearrangements, rather than sequential oxidation and reduction of Y_Z. This reorganization propagates through a dynamic network of hydrogen-bonded water molecules and culminates in redox-coupled deprotonation of the W2 ligand via the Cl1 channel. Our model suggests a long-range coupling mechanism in which Y_Z oxidation drives proton release nearly 18 Å away, mediated by water networks that adaptively respond to—and reshape—the local electrostatic environment.

These findings provide an atomistic explanation for the origin of TR-SFX difference densities during the $S_2 \rightarrow S_3$ transition and offer a structural rationale for the experimentally observed sensitivity of the deprotonation step to Cl^- availability. More broadly, this work highlights the critical role of hydrogen-bond network plasticity in coupling redox chemistry to proton transport, and demonstrates how QM/MM-enhanced MD simulations can extract mechanistic insights from experimental data that remain unresolved at current TR-SFX resolution limits.

METHOD

Quantum Mechanics/Molecular Mechanics

Quantum mechanics/molecular mechanics (QM/MM) models used for geometry optimizations were constructed based on the PSII crystal structure from Umena et al. (PDB ID: 3WU2) as previously described.[32,47] The system contains approximately 2500 atoms, including all residues with Cα atoms within 15 Å of the oxygen-evolving complex (OEC). N-terminal (ACE) and C-terminal (NMA) capping groups were used at the system boundary and held fixed during geometry optimization. The QM region comprises the OEC, one Cl^- ion, 14 water molecules, and selected residues critical for hydrogen bonding and redox coupling: the side chains of D1-D61, D1-Y161, D1-Q165, D1-N181, D1-E189, D1-H190, D1-N298, D1-H332, D1-E333, D1-H337, D1-D342, D1-A344, CP43-E354, CP43-R357, and D2-K317, along with the full residues D1-S169, D1-D170 and D1-G171.[46]

All QM/MM optimizations were performed using the ONIOM method[95] as implemented in Gaussian16.[96] The QM layer was treated with density functional theory (DFT) using the B3LYP exchange−correlation functional.[97−100] LanL2DZ effective core potentials and basis sets were used for Mn and Ca atoms;[101,102] 6−31G(d) was used for O and Cl, and 6−31G for H, C, and N atoms.[103−106] The MM layer was modeled using the AMBER force field.[107] Each intermediate, including States 3A−3F and those in SI, was obtained by stepwise geometry optimization from a previous state, adjusting hydrogen bonds to model the sequential rearrangements. All states are optimized to local minimums unless * is used to label the state with imaginary frequency.

Structure visualization and analysis were performed using GaussView and VMD.[108] All QM/MM-optimized structures are available in the GitHub repository associated with this study.

Molecular Dynamics

System Preparation. MD systems were constructed using psfgen in VMD[108] based on the 1.9 Å-resolution crystal structure of *Thermostichus vulcanus* PSII (PDB ID: 3WU2),[17] with reference to additional PSII structures (PDB IDs: 4V62 and 4UB6).[16,18] Chains A through Z of 3WU2 were used to build a PSII monomer model. Protonation states of titratable residues were assigned using a combination of propKa, MCCE, and manual inspection.[109,110] All resolved MGDG, DGDG, SQDG, and PG lipids were retained. All crystallographic waters were retained, and glycerol oxygen atoms were modeled as water molecules.

The lipid bilayer of PSII was constructed using CHARMM-GUI,[111,112] with the following composition: outer leaflet (MGDG/DGDG/SQDG/PG = 8:4:1:2) and inner leaflet (MGDG/DGDG/SQDG/PG = 8:4:8:1).[113,114] For each lipid type, acyl chain lengths and degrees of unsaturation were assigned according to experimental data.[115] The system was solvated in a rectangular water box containing 62k TIP3P water molecules.[116] 355 Na^+ and 181 Cl^- were added to the system to neutralize and maintain a salt concentration of 0.15 M. The final system has a box dimension of 143 Å × 144 Å × 140Å with 302k atoms.

Force field parameters included CHARMM36m for proteins,[117] CHARMM36 for lipids,[118] and CHARMM36 with updated NBFIX parameters for ions.[119] Cofactor parameters were adopted from Adam et al. and Guerra et al.,[120,121] and parameters for the OEC were assigned as described previously.[47] Because the Mn_4CaO_5 cluster and its immediate ligands were represented by parameters derived from QM/MM fits, the MM description of metal-center dynamics should be regarded as qualitative. These simulations were designed to sample side-chain and hydrogen-bond rearrangements rather than to model bond breaking or proton-coupled electron-transfer events explicitly. Ab initio molecular dynamics would provide a more complete description but is currently limited by system size and computational cost.

MD Protocol. All simulations were performed using NAMD.[122] The system was equilibrated as previously described,[47] and all production runs are carried out with positional restraints of 10 kcal/(mol·Å^2) on the OEC and 2 kcal/(mol·Å^2) on backbone atoms of Y161 and H190 to simplify structural alignment for density calculations (Figure S12). Other necessary restraints are added to the system.[47,123] Temperature was maintained at 310 K using Langevin dynamics (damping coefficient γ = 1.0 ps^{-1}), and pressure was held at 1 atm using an anisotropic Langevin piston barostat.[124] The time step of all simulations was 2 fs, with

https://doi.org/10.1021/jacs.5c13000
J. Am. Chem. Soc. XXXX, XXX, XXX−XXX

bonded interactions and short-range nonbonded interactions (less than the 12-Å cutoff) calculated at every time step. Long-range electrostatics were treated using the particle mesh ewald (PME) method,[125] with grid updates every other time step. All trajectory analyses were performed in VMD.[108] Each restrained trajectory was 10 ns in length. To verify that this sampling was sufficient, we compared positional distributions from the first 5 ns and the full 10 ns, which showed no significant difference in side-chain conformations (Figure S13).

MD-Derived Electron Density Map Generation. Electron density maps were generated from MD trajectories using the CCP4 suite (version 9.0).[126] For each system, 200 snapshots extracted at 50 ps intervals were first aligned using the constrained atoms (OEC, backbone of Y161 and H190). Residues selected for map generation were written to PDB format and processed individually. Each snapshot was converted to a simulated electron density map using sfall with the following parameters: mode atmmap, symm p1, resolution range 120−1.8Å, and isotropic B-factor smearing (BADD 8.0). Framewise maps were summed using mapsig with equal weighting to produce an averaged density map. To calculate difference maps, structure factors were merged using cad, scaled using scaleit, and Fourier-transformed using fft. The resulting maps represent simulated electron density differences between two MD ensembles, and were compared directly with time-resolved XFEL difference maps.

See Supporting Information Text 2 for additional computational details.

■ ASSOCIATED CONTENT

Supporting Information

The Supporting Information is available free of charge at https://pubs.acs.org/doi/10.1021/jacs.5c13000.

Numbering of water molecules; electrostatic environment of the W4 → Y_Z hydrogen bond; Mulliken atomic charges of Y_Z and $Y_Z^{\bullet}$; additional QM/MM-optimized structures; interpretation of O6* density features; energetic evaluation of alternative protonation schemes; TR-SFX features not captured in simulated maps; and additional computational details (PDF)

■ AUTHOR INFORMATION

Corresponding Author

Victor S. Batista − *Department of Chemistry, Yale University, New Haven, Connecticut 06520, United States;* orcid.org/0000-0002-3262-1237; Email: victor.batista@yale.edu

Authors

Jinchan Liu − *Department of Molecular Biophysics and Biochemistry, Yale University, New Haven, Connecticut 06520, United States;* orcid.org/0000-0003-2217-1233

Ke R. Yang − *Key Laboratory of Advanced Energy Materials Chemistry (Ministry of Education), College of Chemistry, Nankai University, Tianjin 300071, China*

Julianne S. Lampert − *Department of Chemistry, Yale University, New Haven, Connecticut 06520, United States;* orcid.org/0009-0007-7386-8600

William H. Armstrong − *Department of Chemistry, Boston College, Chestnut Hill, Massachusetts 02467, United States;* orcid.org/0000-0001-9087-3937

Gary W. Brudvig − *Department of Molecular Biophysics and Biochemistry and Department of Chemistry, Yale University, New Haven, Connecticut 06520, United States;* orcid.org/0000-0002-7040-1892

Complete contact information is available at: https://pubs.acs.org/10.1021/jacs.5c13000

Notes

The authors declare no competing financial interest.

■ ACKNOWLEDGMENTS

We acknowledge financial support from the Division of Chemical Sciences, Geosciences, and Biosciences, Office of Basic Energy Sciences, U.S. Department of Energy, Photosynthetic Systems grants DESC0001423 (to V.S.B.) and DE-FG02-05ER15646 (to G.W.B.). This work was also supported by a generous allocation of high-performance computing time from National Energy Research Scientific Computing Center (NERSC). We thank Jimin Wang (Yale University) and Marilyn Gunner (City University of New York) for insightful discussions.

■ REFERENCES

(1) Nelson, N.; Yocum, C. F. Structure and function of photosystem I and II. *Annu. Rev. Plant Biol.* **2006**, *57*, 521−565.

(2) McEvoy, J. P.; Brudvig, G. W. Water-splitting chemistry of photosystem II. *Chem. Rev.* **2006**, *106*, 4455−4483.

(3) Shen, J. R. The Structure of Photosystem II and the Mechanism of Water Oxidation in Photosynthesis. *Annu. Rev. Plant Biol.* **2015**, *66*, 23−48.

(4) Kok, B.; Forbush, B.; McGloin, M. Cooperation of charges in photosynthetic O_2 evolution-I. A linear four step mechanism. *Photochem. & Photobiol.* **1970**, *11*, 457−475.

(5) Haumann, M.; Liebisch, P.; Müller, C.; Barra, M.; Grabolle, M.; Dau, H. Photosynthetic O_2 formation tracked by time-resolved x-ray experiments. *Science* **2005**, *310*, 1019−1021.

(6) Klauss, A.; Haumann, M.; Dau, H. Alternating electron and proton transfer steps in photosynthetic water oxidation. *Proc. Natl. Acad. Sci. U.S.A.* **2012**, *109*, 16035−16040.

(7) Klauss, A.; Haumann, M.; Dau, H. Seven steps of alternating electron and proton transfer in photosystem II water oxidation traced by time-resolved photothermal beam deflection at improved sensitivity. *J. Phys. Chem. B* **2015**, *119*, 2677−2689.

(8) Dau, H.; Zaharieva, I. Principles, efficiency, and blueprint character of solar-energy conversion in photosynthetic water oxidation. *Acc. Chem. Res.* **2009**, *42*, 1861−1870.

(9) Faunce, T.; et al. Artificial photosynthesis as a frontier technology for energy sustainability. *Energy Environ. Sci.* **2013**, *6*, 1074−1076.

(10) Oliver, T.; Kim, T. D.; Trinugroho, J. P.; Cordón-Preciado, V.; Wijayatilake, N.; Bhatia, A.; Rutherford, A. W.; Cardona, T. The Evolution and Evolvability of Photosystem II. *Annu. Rev. Plant Biol.* **2023**, *74*, 225−257.

(11) Sauer, K.; Yano, J.; Yachandra, V. K. X-ray spectroscopy of the photosynthetic oxygen-evolving complex. *Coord. Chem. Rev.* **2008**, *252*, 318−335.

(12) Pokhrel, R.; Brudvig, G. W. Oxygen-evolving complex of photosystem II: correlating structure with spectroscopy. *Phys. Chem. Chem. Phys.* **2014**, *16*, 11812−11821.

(13) Vinyard, D. J.; Brudvig, G. W. Progress toward a molecular mechanism of water oxidation in photosystem II. *Annu. Rev. Phys. Chem.* **2017**, *68*, 101−116.

(14) Cox, N.; Pantazis, D. A.; Lubitz, W. Current Understanding of the Mechanism of Water Oxidation in Photosystem II and Its Relation to XFEL Data. *Annu. Rev. Plant Biol.* **2020**, *89*, 795−820.

(15) Yano, J.; Kern, J.; Yachandra, V. K. Structure Function Studies of Photosystem II Using X-Ray Free Electron Lasers. *Annu. Rev. Biophys.* **2024**, *53*, 343−365.

(16) Guskov, A.; Kern, J.; Gabdulkhakov, A.; Broser, M.; Zouni, A.; Saenger, W. Cyanobacterial photosystem II at 2.9-Å resolution and the role of quinones, lipids, channels and chloride. *Nat. Struct. Mol. Biol.* **2009**, *16*, 334−342.
(17) Umena, Y.; Kawakami, K.; Shen, J. R.; Kamiya, N. Crystal structure of oxygen-evolving photosystem II at a resolution of 1.9 Å. *Nature* **2011**, *473*, 55−60.
(18) Suga, M.; Akita, F.; Hirata, K.; Ueno, G.; Murakami, H.; Nakajima, Y.; Shimizu, T.; Yamashita, K.; Yamamoto, M.; Ago, H.; Shen, J. R. Native structure of photosystem II at 1.95 Å resolution viewed by femtosecond X-ray pulses. *Nature* **2015**, *517*, 99−103.
(19) Hussein, R.; Graça, A.; Forsman, J.; Aydin, A. O.; Hall, M.; Gaetcke, J.; Chernev, P.; Wendler, P.; Dobbek, H.; Messinger, J.; Zouni, A.; Schröder, W. P. Cryo−electron microscopy reveals hydrogen positions and water networks in photosystem II. *Science* **2024**, *384*, 1349−1355.
(20) Linke, K.; Ho, F. M. Water in photosystem II: structural, functional and mechanistic considerations. *Biochim. Biophys. Acta* **2014**, *1837*, 14−32.
(21) Sakashita, N.; Watanabe, H. C.; Ikeda, T.; Saito, K.; Ishikita, H. Origins of Water Molecules in the Photosystem II Crystal Structure. *Biochemistry* **2017**, *56*, 3049−3057.
(22) Sirohiwal, A.; Pantazis, D. A. Functional water networks in fully hydrated photosystem II. *J. Am. Chem. Soc.* **2022**, *144*, 22035−22050.
(23) Kaur, D.; Reiss, K.; Wang, J.; Batista, V. S.; Brudvig, G. W.; Gunner, M. R. Occupancy Analysis of Water Molecules inside Channels within 25 Å Radius of the Oxygen-Evolving Center of Photosystem II in Molecular Dynamics Simulations. *J. Phys. Chem. B* **2024**, *128*, 2236−2248.
(24) Wincencjusz, H.; van Gorkom, H. J.; Yocum, C. F. The Photosynthetic Oxygen Evolving Complex Requires Chloride for Its Redox State $S_2 \rightarrow S_3$ and $S_3 \rightarrow S_0$ Transitions But Not for $S_0 \rightarrow S_1$ or $S_1 \rightarrow S_2$ Transitions. *Biochemistry* **1997**, *36*, 3663−3670.
(25) Pokhrel, R.; Service, R. J.; Debus, R. J.; Brudvig, G. W. Mutation of Lysine 317 in the D2 Subunit of Photosystem II Alters Chloride Binding and Proton Transport. *Biochemistry* **2013**, *52*, 4758−4773.
(26) Dismukes, G.; Siderer, Y. EPR spectroscopic observations of a manganese center associated with water oxidation in spinach chloroplasts. *FEBS Lett.* **1980**, *121*, 78−80.
(27) Casey, J. L.; Sauer, K. EPR detection of a cryogenically photogenerated intermediate in photosynthetic oxygen evolution. *Biochim. Biophys. Acta − Bioener* **1984**, *767*, 21−28.
(28) Charlot, M.-F.; Boussac, A.; Blondin, G. Towards a spin coupling model for the Mn_4 cluster in Photosystem II. *Biochim. Biophys. Acta − Bioener* **2005**, *1708*, 120−132.
(29) Pantazis, D. A.; Ames, W.; Cox, N.; Lubitz, W.; Neese, F. Two interconvertible structures that explain the spectroscopic properties of the oxygen-evolving complex of photosystem II in the S_2 State. *Angew. Chem., Int. Ed. Engl.* **2012**, *51*, 9935−9940.
(30) Beal, N. J.; Corry, T. A.; O'Malley, P. J. Comparison between Experimental and Broken Symmetry Density Functional Theory (BS-DFT) Calculated Electron Paramagnetic Resonance (EPR) Parameters of the S_2 State of the Oxygen-Evolving Complex of Photosystem II in Its Native (Calcium) and Strontium-Substituted Form. *J. Phys. Chem. B* **2017**, *121*, 11273−11283.
(31) Vinyard, D. J.; Khan, S.; Askerka, M.; Batista, V. S.; Brudvig, G. W. Energetics of the S_2 state spin isomers of the oxygen-evolving complex of photosystem II. *J. Phys. Chem. B* **2017**, *121*, 1020−1025.
(32) Yang, K. R.; Lakshmi, K. V.; Brudvig, G. W.; Batista, V. S. Is deprotonation of the oxygen-evolving complex of photosystem II during the $S_1 \rightarrow S_2$ transitions suppressed by proton quantum delocalization? *J. Am. Chem. Soc.* **2021**, *143*, 8324−8332.
(33) Saito, K.; Mino, H.; Nishio, S.; Ishikita, H. Protonation structure of the closed-cubane conformation of the O_2-evolving complex in photosystem II. *PNAS Nexus* **2022**, *1*, pgac221.
(34) Mermigki, M. A.; Drosou, M.; Pantazis, D. A. On the nature of high-spin forms in the S_2 state of the oxygen-evolving complex. *Chem. Sci.* **2025**, *16*, 4023−4047.
(35) Rappaport, F.; Lavergne, J. Proton release during successive oxidation steps of the photosynthetic water oxidation process: stoichiometries and pH dependence. *Biochemistry* **1991**, *30*, 10004−10012.
(36) Haumann, M.; Hundelt, M.; Jahns, P.; Chroni, S.; Bögershausen, O.; Ghanotakis, D.; Junge, W. Proton release from water oxidation by photosystem II: similar stoichiometries are stabilized in thylakoids and PSII core particles by glycerol. *FEBS Lett.* **1997**, *410*, 243−248.
(37) Sakamoto, H.; Shimizu, T.; Nagao, R.; Noguchi, T. Monitoring the Reaction Process During the $S_2 \rightarrow S_3$ Transition in Photosynthetic Water Oxidation Using Time-Resolved Infrared Spectroscopy. *J. Am. Chem. Soc.* **2017**, *139*, 2022−2029.
(38) Noguchi, T.; Sugiura, M. Flash-induced FTIR difference spectra of the water oxidizing complex in moderately hydrated photosystem II core films: effect of hydration extent on S-state transitions. *Biochemistry* **2002**, *41*, 2322−2330.
(39) Suzuki, H.; Sugiura, M.; Noguchi, T. Monitoring water reactions during the S-state cycle of the photosynthetic water-oxidizing center: detection of the DOD bending vibrations by means of Fourier transform infrared spectroscopy. *Biochemistry* **2008**, *47*, 11024−11030.
(40) Retegan, M.; Cox, N.; Lubitz, W.; Neese, F.; Pantazis, D. A. The first tyrosyl radical intermediate formed in the S_2−S_3 transition of photosystem II. *Phys. Chem. Chem. Phys.* **2014**, *16*, 11901−11910.
(41) Allgöwer, F.; Gamiz-Hernandez, A. P.; Rutherford, A. W.; Kaila, V. R. I. Molecular principles of redox-coupled protonation dynamics in photosystem II. *J. Am. Chem. Soc.* **2022**, *144*, 7171−7180.
(42) Saito, K.; Nishio, S.; Asada, M.; Mino, H.; Ishikita, H. Insights into the protonation state and spin structure for the g = 2 multiline electron paramagnetic resonance signal of the oxygen-evolving complex. *PNAS Nexus* **2023**, *2*, pgad244.
(43) Saito, K.; Chen, Y.; Ishikita, H. Exploring the Deprotonation Process during Incorporation of a Ligand Water Molecule at the Dangling Mn Site in Photosystem II. *J. Phys. Chem. B* **2024**, *128*, 4728−4734.
(44) Allgöwer, F.; Pöverlein, M. C.; Rutherford, A. W.; Kaila, V. R. I. Mechanism of proton release during water oxidation in Photosystem II. *Proc. Natl. Acad. Sci. U.S.A.* **2024**, *121*, No. e2413396121.
(45) Noguchi, T. Mechanism of Proton Transfer through the D1-E65/D2-E312 Gate during Photosynthetic Water Oxidation. *J. Phys. Chem. B* **2024**, *128*, 1866−1875.
(46) Isobe, H.; Shoji, M.; Shen, J.-R.; Yamaguchi, K. Strong coupling between the hydrogen bonding environment and redox chemistry during the S_2 to S_3 transition in the oxygen-evolving complex of photosystem II. *J. Phys. Chem. B* **2015**, *119*, 13922−13933.
(47) Liu, J.; Yang, K. R.; Long, Z.; Armstrong, W. H.; Brudvig, G. W.; Batista, V. S. Water Ligands Regulate the Redox Leveling Mechanism of the Oxygen-Evolving Complex of the Photosystem II. *J. Am. Chem. Soc.* **2024**, *146*, 15986−15999.
(48) Tamura, H.; Saito, K.; Ishikita, H. Electron Transfer Mechanism from the Oxygen-Evolving Complex to the Electron-Acceptor Tyrosine during the S_2 to S_3 Transition in Photosystem II. *ACS Omega* **2025**, *10*, 24461−24471.
(49) Shoji, M.; Isobe, H.; Yamaguchi, K. QM/MM study of the S_2 to S_3 transition reaction in the oxygen-evolving complex of photosystem II. *Chem. Phys. Lett.* **2015**, *636*, 172−179.
(50) Retegan, M.; Krewald, V.; Mamedov, F.; Neese, F.; Lubitz, W.; Cox, N.; Pantazis, D. A. A five-coordinate Mn(IV) intermediate in biological water oxidation: Spectroscopic signature and a pivot mechanism for water binding. *Chem. Sci.* **2016**, *7*, 72−84.
(51) Capone, M.; Narzi, D.; Bovi, D.; Guidoni, L. Mechanism of water delivery to the active site of photosystem II along the S_2 to S_3 Transition. *J. Phys. Chem. Lett.* **2016**, *7*, 592−596.
(52) Li, X.; Siegbahn, P. E.; Ryde, U. Simulation of the isotropic EXAFS spectra for the S_2 and S_3 structures of the oxygen evolving complex in photosystem II. *Proc. Natl. Acad. Sci. U.S.A.* **2015**, *112*, 3979−3984.

https://doi.org/10.1021/jacs.5c13000
J. Am. Chem. Soc. XXXX, XXX, XXX−XXX

(53) Askerka, M.; Wang, J.; Vinyard, D. J.; Brudvig, G. W.; Batista, V. S. S_3 state of the O_2-evolving complex of photosystem II: Insights from QM/MM, EXAFS, and Femtosecond X-ray Diffraction. *Biochemistry* **2016**, *55*, 981−984.
(54) Isobe, H.; Shoji, M.; Shen, J.-R.; Yamaguchi, K. Chemical Equilibrium Models for the S_3 State of the Oxygen-Evolving Complex of Photosystem II. *Inorg. Chem.* **2016**, *55*, 502−511.
(55) Pantazis, D. A. The S_3 State of the Oxygen-Evolving Complex: Overview of Spectroscopy and XFEL Crystallography with a Critical Evaluation of Early-Onset Models for O−O Bond Formation. *Inorganics* **2019**, *7*, 55.
(56) Chrysina, M.; Drosou, M.; Castillo, R. G.; Reus, M.; Neese, F.; Krewald, V.; Pantazis, D. A.; DeBeer, S. Nature of S-States in the Oxygen-Evolving Complex Resolved by High-Energy Resolution Fluorescence Detected X-ray Absorption Spectroscopy. *J. Am. Chem. Soc.* **2023**, *145*, 25579−25594.
(57) Ibrahim, M.; et al. Untangling the sequence of events during the $S_2 \rightarrow S_3$ transition in photosystem II and implications for the water oxidation mechanism. *Proc. Natl. Acad. Sci. U.S.A.* **2020**, *117*, 12624−12635.
(58) Hussein, R.; Ibrahim, M.; Bhowmick, A.; Simon, P. S.; Chatterjee, R.; Lassalle, L.; Doyle, M.; Bogacz, I.; Kim, I. S.; Cheah, M. H.; et al. Structural dynamics in the water and proton channels of photosystem II during the S_2 to S_3 transition. *Nat. Commun.* **2021**, *12*, 6531.
(59) Li, H.; et al. Oxygen-evolving photosystem II structures during S_1−S_2−S_3 transitions. *Nature* **2024**, *626*, 670−677.
(60) Wang, J.; Armstrong, W. H.; Batista, V. S. Do crystallographic XFEL data support binding of a water molecule to the oxygen-evolving complex of photosystem II exposed to two flashes of light? *Proc. Natl. Acad. Sci. U.S.A.* **2021**, *118*, No. e2023982118.
(61) Wang, J. Cryo-EM meets crystallography: A model-independent view of the heteronuclear Mn_4Ca cluster structure of photosystem II. *Proc. Natl. Acad. Sci. U.S.A.* **2025**, *122*, No. e2423012122.
(62) Sproviero, E. M.; Gascón, J. A.; McEvoy, J. P.; Brudvig, G. W.; Batista, V. S. Quantum Mechanics/Molecular Mechanics Study of the Catalytic Cycle of Water Splitting in Photosystem II. *J. Am. Chem. Soc.* **2008**, *130*, 3428−3442.
(63) Siegbahn, P. E. M. Structures and Energetics for O_2 Formation in Photosystem II. *Acc. Chem. Res.* **2009**, *42*, 1871−1880.
(64) Kern, J.; et al. Structures of the intermediates of Kok's photosynthetic water oxidation clock. *Nature* **2018**, *563*, 421−425.
(65) Kawashima, K.; Takaoka, T.; Kimura, H.; Saito, K.; Ishikita, H. O_2 evolution and recovery of the water-oxidizing enzyme. *Nat. Commun.* **2018**, *9*, 1247.
(66) Zhang, B.; Sun, L. Why nature chose the Mn_4CaO_5 cluster as water-splitting catalyst in photosystem II: a new hypothesis for the mechanism of O−O bond formation. *Dalton Trans.* **2018**, *47*, 14381−14387.
(67) Suga, M.; et al. An oxyl/oxo mechanism for oxygen-oxygen coupling in PSII revealed by an x-ray free-electron laser. *Science* **2019**, *366*, 334−338.
(68) Guo, Y.; Messinger, J.; Kloo, L.; Sun, L. Alternative Mechanism for O_2 Formation in Natural Photosynthesis via Nucleophilic Oxo−Oxo Coupling. *J. Am. Chem. Soc.* **2023**, *145*, 4129−4141.
(69) Greife, P.; Schönborn, M.; Capone, M.; Assunção, R.; Narzi, D.; Guidoni, L.; Dau, H. The electron−proton bottleneck of photosynthetic oxygen evolution. *Nature* **2023**, *617*, 623−628.
(70) Bhowmick, A.; et al. Structural evidence for intermediates during O_2 formation in photosystem II. *Nature* **2023**, *617*, 629−636.
(71) Guo, Y.; He, L.; Ding, Y.; Kloo, L.; Pantazis, D. A.; Messinger, J.; Sun, L. Closing Kok's cycle of nature's water oxidation catalysis. *Nat. Commun.* **2024**, *15*, 5982.
(72) Metz, J. G.; Nixon, P. J.; Rogner, M.; Brudvig, G. W.; Diner, B. A. Directed alteration of the D1 polypeptide of photosystem II: evidence that tyrosine-161 is the redox component, Z, connecting the oxygen-evolving complex to the primary electron donor, P680. *Biochemistry* **1989**, *28*, 6960−6969.
(73) Styring, S.; Sjöholm, J.; Mamedov, F. Two tyrosines that changed the world: interfacing the oxidizing power of photochemistry to water splitting in photosystem II. *Biochim. Biophys. Acta − Bioener* **2012**, *1817*, 76−87.
(74) Eckert, H.-J.; Renger, G. Temperature dependence of $P680^+$ reduction in O_2-evolving PS II membrane fragments at different redox states S_i of the water oxidizing system. *FEBS Lett.* **1988**, *236*, 425−431.
(75) Kühn, P.; Eckert, H.-J.; Eichler, H. J.; Renger, G. Analysis of the $P680^{+\cdot}$ reduction pattern and its temperature dependence in oxygen-evolving PS II core complexes from thermophilic cyanobacteria and higher plants. *Phys. Chem. Chem. Phys.* **2004**, *6*, 4838−4843.
(76) Renger, G. Mechanism of light induced water splitting in Photosystem II of oxygen evolving photosynthetic organisms. *Biochim. Biophys. Acta − Bioener* **2012**, *1817*, 1164−1176.
(77) Nakamura, S.; Nagao, R.; Takahashi, R.; Noguchi, T. Fourier Transform Infrared Detection of a Polarizable Proton Trapped between Photooxidized Tyrosine Y_Z and a Coupled Histidine in Photosystem II: Relevance to the Proton Transfer Mechanism of Water Oxidation. *Biochemistry* **2014**, *53*, 3131−3144.
(78) Nakamura, S.; Capone, M.; Narzi, D.; Guidoni, L. Pivotal role of the redox-active tyrosine in driving the water splitting catalyzed by photosystem II. *Phys. Chem. Chem. Phys.* **2020**, *22*, 273−285.
(79) Rappaport, F.; Diner, B. A. Primary photochemistry and energetics leading to the oxidation of the $(Mn)_4Ca$ cluster and to the evolution of molecular oxygen in Photosystem II. *Coord. Chem. Rev.* **2008**, *252*, 259−272.
(80) Mandal, M.; Kawashima, K.; Saito, K.; Ishikita, H. Redox Potential of the Oxygen-Evolving Complex in the Electron Transfer Cascade of Photosystem II. *J. Phys. Chem. Lett.* **2020**, *11*, 249−255.
(81) Tamura, H.; Saito, K.; Nishio, S.; Ishikita, H. Electron-Transfer Route in the Early Oxidation States of the Mn_4CaO_5 Cluster in Photosystem II. *J. Phys. Chem. B* **2023**, *127*, 205−211.
(82) Zaharieva, I.; Dau, H.; Haumann, M. Sequential and Coupled Proton and Electron Transfer Events in the $S_2 \rightarrow S_3$ Transition of Photosynthetic Water Oxidation Revealed by Time-Resolved X-ray Absorption Spectroscopy. *Biochemistry* **2016**, *55*, 6996−7004.
(83) Sugie, K.; Kato, Y.; Nagao, R.; Noguchi, T. Mechanism of the Oxygen-Evolving Process in the Water-Oxidizing Complex of Photosystem II, as Revealed by Time-Resolved Infrared Spectroscopy. *J. Phys. Chem. B* **2025**, *129*, 6172−6187.
(84) Rappaport, F.; Blanchard-Desce, M.; Lavergne, J. Kinetics of electron transfer and electrochromic change during the redox transitions of the photosynthetic oxygen-evolving complex. *Biochim. Biophys. Acta − Bioener* **1994**, *1184*, 178−192.
(85) Babcock, G. E. T.; Blankenship, R.; Sauer, K. Reaction kinetics for positive charge accumulation on the water side of choloplast photosystem II. *FEBS Lett.* **1976**, *61*, 286−289.
(86) Dau, H.; Haumann, M. The manganese complex of photosystem II in its reaction cycle—Basic framework and possible realization at the atomic level. *Coord. Chem. Rev.* **2008**, *252*, 273−295.
(87) Dwyer, J. J.; Gittis, A. G.; Karp, D. A.; Lattman, E. E.; Spencer, D. S.; Stites, W. E.; García-Moreno E, B. High Apparent Dielectric Constants in the Interior of a Protein Reflect Water Penetration. *Biophys. J.* **2000**, *79*, 1610−1620.
(88) Bone, S.; Pethig, R. Dielectric studies of the binding of water to lysozyme. *J. Mol. Biol.* **1982**, *157*, 571−575.
(89) Soper, A. The radial distribution functions of water and ice from 220 to 673 K and at pressures up to 400 MPa. *Chem. Phys.* **2000**, *258*, 121−137.
(90) Kaur, D.; Szejgis, W.; Mao, J.; Amin, M.; Reiss, K. M.; Askerka, M.; Cai, X.; Khaniya, U.; Zhang, Y.; Brudvig, G. W.; Batista, V. S.; Gunner, M. R. Relative stability of the S_2 isomers of the oxygen evolving complex of photosystem II. *Photosyn. Res.* **2019**, *141*, 331−341.
(91) Gisriel, C. J.; Wang, J.; Liu, J.; Flesher, D. A.; Reiss, K. M.; Huang, H.-L.; Yang, K. R.; Armstrong, W. H.; Gunner, M. R.; Batista, V. S.; Debus, R. J.; Brudvig, G. W. High-resolution cryo-electron microscopy structure of photosystem II from the mesophilic

https://doi.org/10.1021/jacs.5c13000
J. Am. Chem. Soc. XXXX, XXX, XXX−XXX

cyanobacterium, *Synechocystis* sp. PCC 6803. *Proc. Natl. Acad. Sci. U.S.A.* **2022**, *119*, No. e2116765118.
(92) Flesher, D. A.; Debus, R. J.; Brudvig, G. W. Structure of the D1-Val185Asn Mutated Photosystem II Complex with Slow O−O Bond Formation Reveals Changes in the Cl1 Water Channel. *Proc. Natl. Acad. Sci. U.S.A.* **2025**, *122*, No. e2522652122.
(93) Kim, C. J.; Debus, R. J. One of the Substrate Waters for O_2 Formation in Photosystem II Is Provided by the Water-Splitting Mn_4CaO_5 Cluster's Ca^{2+} Ion. *Biochemistry* **2019**, *58*, 3185−3192.
(94) Amin, M.; Vogt, L.; Vassiliev, S.; Rivalta, I.; Sultan, M. M.; Bruce, D.; Brudvig, G. W.; Batista, V. S.; Gunner, M. R. Electrostatic Effects on Proton Coupled Electron Transfer in Oxomanganese Complexes Inspired by the Oxygen-Evolving Complex of Photosystem II. *J. Phys. Chem. B* **2013**, *117*, 6217−6226.
(95) Vreven, T.; Morokuma, K. The ONIOM (our own N-layered integrated molecular orbital + molecular mechanics) method for the first singlet excited (S_1) state photoisomerization path of a retinal protonated Schiff base. *J. Chem. Phys.* **2000**, *113*, 2969−2975.
(96) Frisch, M. J.; et al. *Gaussian 16* Revision C.01. 2016; Gaussian Inc: Wallingford CT.
(97) Becke, A. D. Density-functional thermochemistry. III. The role of exact exchange. *J. Chem. Phys.* **1993**, *98*, 5648−5652.
(98) Lee, C.; Yang, W.; Parr, R. G. Development of the Colle-Salvetti correlation-energy formula into a functional of the electron density. *Phys. Rev. B* **1988**, *37*, 785−789.
(99) Vosko, S. H.; Wilk, L.; Nusair, M. Accurate spin-dependent electron liquid correlation energies for local spin density calculations: a critical analysis. *Can. J. Phys.* **1980**, *58*, 1200−1211.
(100) Stephens, P. J.; Devlin, F. J.; Chabalowski, C. F.; Frisch, M. J. Ab Initio Calculation of Vibrational Absorption and Circular Dichroism Spectra Using Density Functional Force Fields. *J. Phys. Chem.* **1994**, *98*, 11623−11627.
(101) Hay, P. J.; Wadt, W. R. Ab initio effective core potentials for molecular calculations. Potentials for K to Au including the outermost core orbitals. *J. Chem. Phys.* **1985**, *82*, 299−310.
(102) da Silva Filho, D. A.; Coropceanu, V.; Fichou, D.; Gruhn, N. E.; Bill, T. G.; Gierschner, J.; Cornil, J.; Brédas, J.-L. Hole-vibronic coupling in oligothiophenes: impact of backbone torsional flexibility on relaxation energies. *Philos. Trans. R. Soc. A* **2007**, *365*, 1435−1452.
(103) Hariharan, P. C.; Pople, J. A. The influence of polarization functions on molecular orbital hydrogenation energies. *Theoret. Chim. Acta* **1973**, *28*, 213−222.
(104) Sproviero, E. M.; Gascon, J. A.; McEvoy, J. P.; Brudvig, G. W.; Batista, V. S. Characterization of synthetic oxomanganese complexes and the inorganic core of the O_2-evolving complex in photosystem II: evaluation of the DFT/B3LYP level of theory. *J. Inorg. Biochem.* **2006**, *100*, 786−800.
(105) Wang, T.; Brudvig, G.; Batista, V. S. Characterization of proton coupled electron transfer in a biomimetic oxomanganese complex: Evaluation of the DFT B3LYP level of theory. *J. Chem. Theory Comput.* **2010**, *6*, 755−760.
(106) Luo, S.; Rivalta, I.; Batista, V.; Truhlar, D. G. Noncollinear Spins Provide a Self-Consistent Treatment of the Low-Spin State of a Biomimetic Oxomanganese Synthetic Trimer Inspired by the Oxygen Evolving Complex of Photosystem II. *J. Phys. Chem. Lett.* **2011**, *2*, 2629−2633.
(107) Cornell, W. D.; Cieplak, P.; Bayly, C. I.; Gould, I. R.; Merz, K. M.; Ferguson, D. M.; Spellmeyer, D. C.; Fox, T.; Caldwell, J. W.; Kollman, P. A. A Second Generation Force Field for the Simulation of Proteins, Nucleic Acids, and Organic Molecules. *J. Am. Chem. Soc.* **1995**, *117*, 5179−5197.
(108) Humphrey, W.; Dalke, A.; Schulten, K. VMD − Visual Molecular Dynamics. *J. Mol. Graphics* **1996**, *14*, 33−38.
(109) Bas, D. C.; Rogers, D. M.; Jensen, J. H. Very fast prediction and rationalization of pKa values for protein-ligand complexes. *Proteins* **2008**, *73*, 765−783.
(110) Kaur, D.; Zhang, Y.; Reiss, K. M.; Mandal, M.; Brudvig, G. W.; Batista, V. S.; Gunner, M. Proton exit pathways surrounding the oxygen evolving complex of photosystem II. *Biochim. Biophys. Acta − Bioener.* **2021**, *1862*, 148446.
(111) Lee, J.; et al. CHARMM-GUI Membrane Builder for Complex Biological Membrane Simulations with Glycolipids and Lipoglycans. *J. Chem. Theory Comput.* **2019**, *15*, 775−786.
(112) Li, Y.; Liu, J.; Gumbart, J. C. In *Structure and Function of Membrane Proteins*; Schmidt-Krey, I., Gumbart, J. C., Eds.; Springer US: New York, NY, 2021; pp 237−251.
(113) Staehelin, L. A.; van der Staay, G. W. M. *Oxygenic Photosynthesis: The Light Reactions*; Springer Netherlands: Dordrecht, 1996; pp 11−30.
(114) Mizusawa, N.; Wada, H. The role of lipids in photosystem II. *Biochim. Biophys. Acta − Bioener* **2012**, *1817*, 194−208.
(115) Sakurai, I.; Shen, J.-R.; Leng, J.; Ohashi, S.; Kobayashi, M.; Wada, H. Lipids in oxygen-evolving photosystem II complexes of cyanobacteria and higher plants. *J. Biochem.* **2006**, *140*, 201−209.
(116) Jorgensen, W. L.; Chandrasekhar, J.; Madura, J. D.; Impey, R. W.; Klein, M. L. Comparison of simple potential functions for simulating liquid water. *J. Chem. Phys.* **1983**, *79*, 926−935.
(117) Huang, J.; Rauscher, S.; Nawrocki, G.; Ran, T.; Feig, M.; de Groot, B. L.; Grubmüller, H.; MacKerell, A. D. CHARMM36m: an improved force field for folded and intrinsically disordered proteins. *Nat. Methods* **2017**, *14*, 71−73.
(118) Klauda, J. B.; Venable, R. M.; Freites, J. A.; O'Connor, J. W.; Tobias, D. J.; Mondragon-Ramirez, C.; Vorobyov, I.; MacKerell, A. D.; Pastor, R. W. Update of the CHARMM all-atom additive force field for lipids: validation on six lipid types. *J. Phys. Chem. B* **2010**, *114*, 7830−7843.
(119) Venable, R. M.; Luo, Y.; Gawrisch, K.; Roux, B.; Pastor, R. W. Simulations of Anionic Lipid Membranes: Development of Interaction-Specific Ion Parameters and Validation Using NMR Data. *J. Phys. Chem. B* **2013**, *117*, 10183−10192.
(120) Adam, S.; Knapp-Mohammady, M.; Yi, J.; Bondar, A.-N. Revised CHARMM force field parameters for iron-containing cofactors of photosystem II. *J. Comput. Chem.* **2018**, *39*, 7−20.
(121) Guerra, F.; Adam, S.; Bondar, A.-N. Revised force-field parameters for chlorophyll-a, pheophytin-a and plastoquinone-9. *J. Mol. Graph. Model.* **2015**, *58*, 30−39.
(122) Phillips, J. C.; Braun, R.; Wang, W.; Gumbart, J.; Tajkhorshid, E.; Villa, E.; Chipot, C.; Skeel, R. D.; Kale, L.; Schulten, K. Scalable molecular dynamics with NAMD. *J. Comput. Chem.* **2005**, *26*, 1781−1802.
(123) Ishikita, H.; Saito, K. Proton transfer reactions and hydrogen-bond networks in protein environments. *J. R. Soc. Interface* **2014**, *11*, 20130518.
(124) Martyna, G. J.; Tobias, D. J.; Klein, M. L. Constant pressure molecular dynamics algorithms. *J. Chem. Phys.* **1994**, *101*, 4177−4189.
(125) Darden, T.; York, D.; Pedersen, L. Particle mesh Ewald: An N·log (N) method for Ewald sums in large systems. *J. Chem. Phys.* **1993**, *98*, 10089−10092.
(126) Agirre, J.; et al. The CCP4 suite: integrative software for macromolecular crystallography. *Acta Crystallogr. D: Struct. Biol.* **2023**, *79*, 449−461.

https://doi.org/10.1021/jacs.5c13000
J. Am. Chem. Soc. XXXX, XXX, XXX−XXX